Investigation of Hamamatsu H8500 phototubes as single photon detectors.

M. Hoek[c], V. Lucherini[a], M. Mirazita[a], R.A. Montgomery[a], A. Orlandi[a], S. Anefalos Pereira[a], S. Pisano[a], P. Rossi[a,b], A. Viticchiè[a], A. Witchger[d]

[a] *INFN Laboratori Nazionali di Frascati, Via Enrico Fermi, 40, 00044 Frascati, Italy*
[b] *Jefferson Laboratory, Thomas Jefferson National Accelerator Facility, 12000 Jefferson Avenue, Newport News, VA 23606, USA*
[c] *Institut für Kernphysik, Johannes Gutenberg-Universität Mainz, Johann-Joachim-Becher-Weg 45, D 55128 Mainz, Germany*
[d] *Department of Physics, North Carolina State University, 2401 Stinson Drive, Raleigh, NC 27695-8202, USA*

Abstract

We have investigated the response of a significant sample of Hamamatsu H8500 MultiAnode PhotoMultiplier Tubes (MAPMTs) as single photon detectors, in view of their use in a ring imaging Cherenkov counter for the CLAS12 spectrometer at the Thomas Jefferson National Accelerator Facility. For this, a laser working at 407.2 nm wavelength was employed. The sample is divided equally into standard window type, with a spectral response in the visible light region, and UV-enhanced window type MAPMTs. The studies confirm the suitability of these MAPMTs for single photon detection in such a Cherenkov imaging application.

Keywords: Photon Detection, PMT, MAPMT, Multianode Photomultiplier Tube, Hamamatsu, H8500, RICH, Cherenkov, CLAS12, JLab

1. Introduction

The CEBAF electron accelerator of the Thomas Jefferson National Accelerator Facility (TJNAF), in Newport News (VA, USA), is currently undergoing an upgrade to increase its maximum energy from 6 to 12 GeV [1]. In the experimental Hall-B, the CLAS spectrometer [2] is being modified and upgraded to CLAS12 [3], in order to operate in the new experimental conditions. The major focus of the Hall-B physics program at 12 GeV will be the study of the internal dynamics and 3-dimensional imaging of the nucleon, quark hadronization processes, and kaon versus pion production in hard exclusive and semi-inclusive scattering, to provide access to the flavour decomposition of the non-perturbative distribution functions.

The main features of CLAS12 are its capability to operate at high luminosities (on the order of $10^{35}\ cm^{-2}s^{-1}$), and operation of highly polarized beam and nucleon targets. The design of the CLAS12 spectrometer is described in [3]. The spectrometer in its present configuration does not provide an efficient kaon identification at large momenta, from 3 - 8 GeV/c. At such momenta, the semi-inclusive kaon yield is one order of magnitude smaller than the pion yield. The required rejection factor for pions is then around 1 : 500, corresponding to a $4\,\sigma$ pion-kaon separation for a contamination in the kaon sample of a few percent. Moreover the baseline spectrometer detectors do not allow the separation of positive kaons from protons in the $5-8$ GeV/c momentum interval.

Improved particle identification and event reconstruction can be achieved in this momentum range by replacing the foreseen low-threshold Cherenkov counter with a Ring Imaging CHerenkov (RICH) detector, without any impact on the baseline design of CLAS12. A study for a RICH detector to be implemented within the CLAS12 spectrometer is reported in [4]. It is shown that, using aerogel radiators, it is possible to achieve the required identification of kaons up to 8 GeV/c momenta if the photon detector employed has a spatial resolution less than than 1 cm^2. In this respect, a possible choice is that of Multi-Anode PhotoMultiplier Tubes (MAPMTs) having single photon detection capabilities.

This paper describes a set of experimental tests which were performed at the Laboratori Nazionali di Frascati (LNF) to measure the response of Hamamatsu H8500 MAPMTs to photons in the blue wavelength region, in order to assess their performance as single photon detectors to be used in a RICH counter. This wavelength was selected to match with the peak intensity of useful Cherenkov radiation produced in aerogel (UV-visible region). For the first time, a large sample of H8500 MAPMTs has been tested, and the variation between their responses assessed. Moreover, two different H8500 MAPMT types have been tested: both the standard and the UV-enhanced window types (14 units of each).

2. The Hamamatsu H8500

The Hamamatsu H8500 is a multianode bialkali photomultiplier tube, comprised of 8×8 pixels and having a 12-stage amplification. The external size is $52 \times 52\,mm^2$, with an active area of $49 \times 49\,mm^2$ and a high packing fraction of 89 %. Each pixel is a square of 5.8 mm length sides and the device has a pixel-to-pixel pitch of 6.08 mm, providing an imaging plane with small dead-space. Two versions of such MAPMT are available: the H8500C type, with spectral response in the visible light range from 300 to 650 nm wavelengths; and the H8500C-03 type, with enhanced response in the UV region, from 185 to 650 nm. For both MAPMTs, the peak efficiency is at a wavelength of about 400 nm, in the blue light region, where the quantum efficiency is around 30 %. The High Voltage (HV) supply range recommended by Hamamatsu is between -900 V and -1100 V, with a reference value of -1000 V [5]. Hamamatsu measured various relevant parameters of the phototubes at this reference voltage, some of which are reported in Tab. 1 for the 14 H8500C and 14 H8500C-03 MAPMTs that we tested.

The MAPMTs are very low noise devices, with small dark currents, and the expected dark count rates for each of the MAPMTs, as calculated from the dark currents measured by Hamamatsu, are also given in Tab. 1. These rates were used to calculate the expected background from dark noise in the MAPMTs in the CLAS12 RICH detector and was concluded to be negligible, with a mean probability of $\sim 3{\times}10^{-4}$ dark counts expected from each MAPMT per CLAS12 detector data acquisition time window of 250 ns. The dark noise behaviour of the MAPMTs is therefore not considered to cause any concern for their application in the CLAS12 RICH detector and therefore we do not discuss this topic any further.

For later reference, we show in Fig. 1 the numbering scheme from Hamamatsu for the 64 pixels of the H8500, as seen by looking at the entrance window of the MAPMT.

3. The Test Set-up

We tested the response of the H8500 MAPMTs reported in Tab. 1 to a low intensity laser beam, at the LNF. The test set-up included a laser emitting blue light (in the region close to where the

Table 1: Selected characteristics of the 28 H8500 MAPMTs used in the tests, according to the Hamamatsu data sheets and as measured at HV= -1000 V. The expected dark count rates of each MAPMT, as calculated from the dark current values measured by Hamamatsu, are also given.

ID	type	Serial no.	Dark current (nA)	Dark count rate (kHz)	Gain (10^6)
1	H8500C	CA4655	4.23	9.01	2.93
2		CA4658	0.16	0.53	1.89
3		CA4667	0.09	0.39	1.45
4		CA4683	0.24	0.89	1.69
5		CA4686	1.20	2.87	2.61
6		CA5342	0.27	0.60	2.81
7		CA5348	0.12	0.27	2.73
8		CA5525	0.29	0.69	2.64
9		CA5562	0.24	0.70	2.15
10		CA5575	0.50	1.12	2.70
11		CA5577	0.25	0.38	4.10
12		CA5675	1.44	3.26	2.76
13		CA5683	0.20	0.45	2.78
14		CA5687	0.91	3.30	1.72
15	H8500C-03	DA0168	0.16	0.36	2.78
16		DA0172	0.17	0.77	1.37
17		DA0174	0.73	2.16	2.11
18		DA0179	0.24	0.83	1.81
19		DA0181	0.12	0.44	1.71
20		DA0348	0.23	0.71	2.01
21		DA0349	0.47	0.98	2.99
22		DA0353	0.17	0.70	1.52
23		DA0355	0.16	0.66	1.52
24		DA0356	0.12	0.26	2.84
25		DA0357	0.17	0.35	3.03
26		DA0359	0.14	0.38	2.29
27		DA0360	0.29	0.48	3.81
28		DA0361	0.39	0.67	3.64

Hamamatsu H8500 MAPMT has its maximal quantum efficiency) and standard VME electronics for the readout. Two motorised step motors were also employed to remotely move the laser beam across the MAPMT entrance window. The set-up was installed inside a light-tight box to isolate the MAPMT from any background light, as shown in Fig. 2.

3.1. The Laser and Motors

For the light source we used a PiLas picosecond injection laser [6], a compact system based on a laser diode, emitting monochromatic light at the wavelength of 407.2 nm. The light was transported from the laser diode to inside the light-tight box via a fiber-optical cable of 1 mm diameter. A 1 mm diameter, 50 mm long PVC custom-made mechanical collimator was inserted onto the lens collimator at the end of the fiber-optical cable and then mounted onto a mechanical

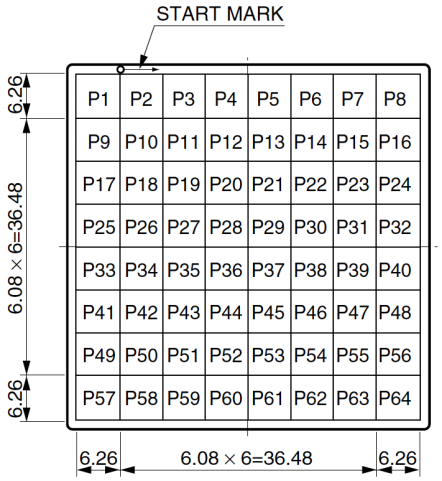

Figure 1: Numbering of the 64 pixels of an H8500 MAPMT, as seen by looking towards the entrance window (front view). Image taken from [5]. The dimensions of the MAPMT are also marked.

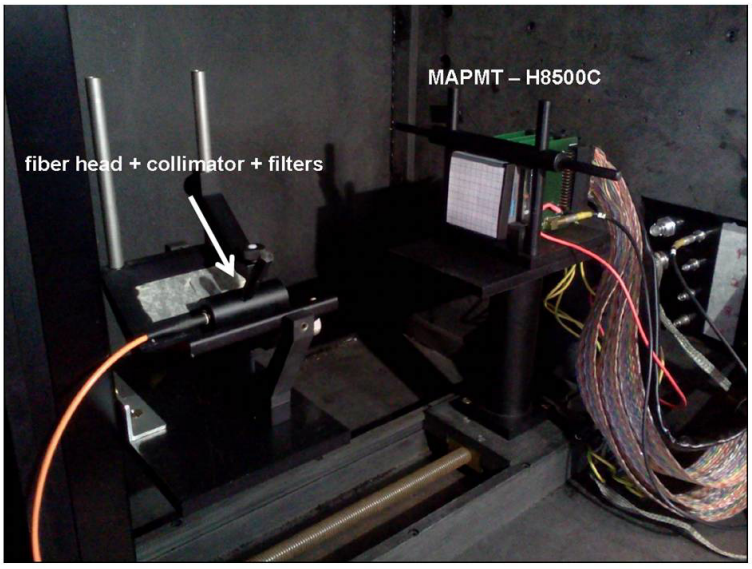

Figure 2: The set-up used for tests of the Hamamatsu H8500 MAPMTs, inside the light-tight box.

support which was driven by two high precision motors from Thorlabs [7] (one for each of the horizontal and vertical movements). The motors were remotely controlled so that the support could be moved across the entire surface of the MAPMT entrance window and illuminate each by each of all its 64 pixels. With this set-up it was possible to perform automised scans of the response of all pixels of each MAPMT. The intensity of the laser beam was reduced down to the level of a few photons per pulse by using neutral optical density filters [8], which were mounted after the collimator. Finer adjustments were possible by changing the settings of the laser tune (relative intensity) on its controller unit, allowing to vary the photon intensity within the linear range of its performance. The tests were done typically with the filters having a total attenuation factor on the order of $\approx 10^6$ and a laser tune setting of $\approx 25\,\%$. The pulse repetition rate was driven by and controlled by the Data AcQuisition (DAQ) readout program and was set to 100 Hz for the duration of the tests.

3.2. Electronics

We used standard VME electronics to read the 64 anodes of one H8500 at a time. A CAEN V2718 VME Bridge, connected to a computer via an optical fiber, was used to generate the *Trigger In* signal for the PiLas. After arrival of this *Trigger In* signal and before emitting the light pulses, the PiLas controller generated a TTL *Trigger Out* signal that, reshaped through a CAEN 89 NIM/TTL converter and stretched to a length of 40 ns through a CAEN N93B Dual Timer, was used as the gate signal for the readout of two CAEN V792 QDCs. The CAEN V792 QDC is a fast, 32 channel charge - to - digital converter with a dynamical range of 400 pC and an upper resolution of ≈ 100 fC. The analogue signals of all the 64 pixels of an MAPMT were extracted through custom designed readout boards and then sent to the QDCs using four 16-channel flat-ribbon cables.

Having the goal of measuring QDC spectra in the few PhotoElectron (p.e.) regime, it was extremely important to check the noise level of the electronics. For this, we ran for several hours with the entire set-up in its operating conditions, but with the surface of the MAPMT covered by a black cap, so that no light could reach the photocathode. The result for a representative pixel of one of the tested MAPMTs is shown in Fig. 3. We can see a very sharp and narrow distribution of the electronic noise pedestal and, over several orders of magnitudes, almost no background hits beyond this pedestal were recorded. The probability to have a noise signal $3\,\sigma$ outside the pedestal peak is calculated as less than $\sim 10^{-6}$ - 10^{-7}. Similar results were found for all the pixels of all the MAPMTs. The behaviour also reflects the low dark-noise characteristics of the MAPMTs, as listed in Tab. 1, and confirms that background noise from the MAPMTs are not expected to be an issue for their application in the CLAS12 RICH detector. The pedestal distributions were extremely narrow, indicating a very low noise set-up which was suitable for the single photon tests. Overall, the RMS values of their distributions were about 0.5 QDC channels, corresponding to $5{\times}10^{-2}$ pC of integrated charge.

3.3. MAPMT Scan Method

Before starting the systematic study of the response of all MAPMTs, a single MAPMT was selected to perform a finer scan of some typical pixels with a laser spot of diameter $90\,\mu$m and step size of 0.1 mm in both directions, in order to verify the uniformity of the response across its pixels' surfaces [9]. The response across the pixel active area was found to be sufficiently homogeneous and uniform for the CLAS12 RICH application. Furthermore, the MAPMT pixel size and dead-space regions measured by the fine scans were as expected, fulfilling the position

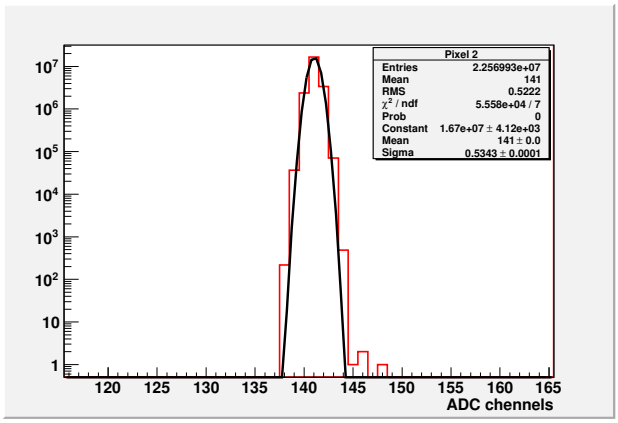

Figure 3: Pedestal measurement for a representative pixel of one MAPMT after several hours of continuous data taking at HV = -1000 V. The MAPMT entrance window was covered with a black cap and the set-up put inside the light-tight box. The results confirm both the low noise environment of the set-up and the small dark noise behaviour of the MAPMTs.

resolution requirement of the RICH detector. From these tests it was concluded that a coarser resolution scan could be employed to test the high statistics sample of MAPMTs.

The tests of the 28 MAPMTs have been performed using an automated procedure, in which a pedestal run (with laser off) was performed first; then the laser head was moved to illuminate the centre of the first pixel (the one at the top-left), the laser was switched on and a 10 k event-sized measurement for all the 64 pixels simultaneously was taken. After that, the laser was moved to illuminate the centre of the next pixel, and a new measurement was done on all the pixels, and so on. At the end of the 64^{th} measurement with the laser on, with the head illuminating the centre of the last pixel (the one at the bottom-right), the laser was switched off and a new pedestal run was performed to check the stability of the electronics. With this procedure, we were able to study the entire MAPMT response when a single pixel was illuminated by the laser and also when the pixel was not illuminated, the latter condition providing useful information on the cross talk between channels.

3.4. QDC Spectra Analysis

The analysis of the data have been performed following the method described in [10]. For this, the QDC spectrum measured by each pixel has been fitted using Equation 1, where q is the QDC channel readout and $P(q)$ and $G_k(q)$ are functions (normalised to 1) describing the shape of the pedestal and of the k^{th} p.e. peak, respectively.

$$f(q) = A\left[e^{-\mu}P(q) + \sum_{k=1}^{N}\frac{\mu^k e^{-\mu}}{k!}G_k(q)\right] \tag{1}$$

Each term in the sum is weighted by the Poisson distribution having $k = 0, 1, 2, ..., N$ p.e., with μ being the average number of detected p.e.. The parameter A represents a normalisation constant term that, since all the factors in the sum are normalised to one, gives the total number of recorded events. The mean position Q_k and sigma width S_k of the k^{th} p.e. peak, for $k > 1$, are computed as

$Q_k = Q_1 + (k-1) \times d$ and $S_k = \sqrt{k} S_1$, where: Q_1 is the mean position of the first p.e. peak; d is the distance between successive p.e. peaks; S_1 is the sigma width of the first p.e. peak. Typically, the average number of detected *p.e.* was $\mu < 1$, so that the total number of *p.e.* peaks considered in the fit was chosen to be 5. The fit description used was slightly simplified with respect to the full possible model given in [10], which may include contributions from different background effects, such as photon conversions on the first dynode stage of the MAPMT for example. This was due mostly to the relatively low resolution of the QDC spectra, in conjunction with the fact that the relation given in Equation 1 was found to describe the spectra well, whilst also providing the most successful automisation and convergence of the fits. For the narrow pedestals measured (see Fig. 3) a simple Gaussian model was used, while for the *p.e.* peaks several different parametrizations have been tried. It was found that the best results (in terms of convergence of the fits and of uniformity of the function parameters) were obtained using Gaussian distributions as well, even though other shapes could provide in some cases slightly better values of χ^2.

4. Results at the Nominal Supply Voltage

Our first test was to check the average gain values quoted by Hamamatsu at the reference supply voltage of HV = -1000 V (see Tab. 1). Two representative QDC spectra are shown in Fig. 4 for the CA4658 MAPMT, measured with the laser illuminating the selected pixels. In

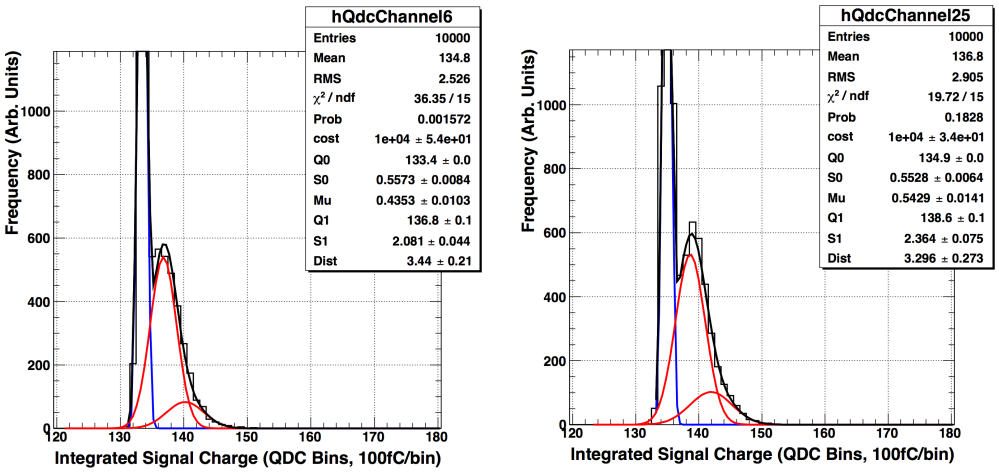

(a) Pixel 25 (b) Pixel 36

Figure 4: Two representative QDC spectra for pixels 25 and 36 of the CA4658 MAPMT at HV=-1000 V (the pixel numbers mapped to electronic QDC readout channels 6 and 25 respectively). The curves show the total fit (black), the pedestal (blue) and *p.e.* (red) contributions. The results for the free parameters of the fits may also be read in the plots, where: *cost* is the normalisation constant (A); $Q0$ and $S0$ are the mean and sigma width of the pedestal Gaussian distribution; *Mu* is μ, the average number of detected p.e.; $Q1$ and $S1$ are the mean and sigma width of the first p.e. Gaussian distribution; *Dist* is d, the distance between the p.e. peaks.

each of the plots of Figs. 4 (a) and (b) the overall results of the fits are shown (black curve), together with the individual contributions (pedestal in blue and the *p.e.* peaks in red). Since the

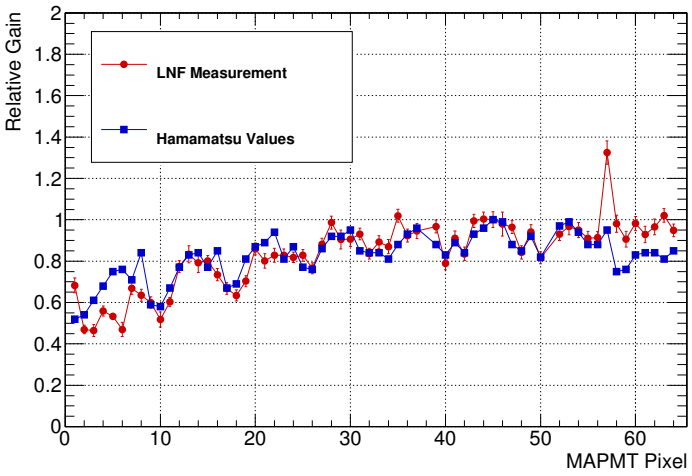

Figure 5: Comparison between the gains of all 64 pixels of the CA4658 MAPMT at HV=-1000 V as given by Hamamatsu (blue squares) and as extracted from fits to the measured spectra (red circles). In both cases, the values have been normalised to the gain of the highest pixel.

average number of detected *p.e.* is $\mu \approx 0.5$, the gaussian contributions for $k > 2$ *p.e.* are relatively small.

According to the Hamamatsu data sheet, pixel 36 (Fig. 4 (b)) has a gain about 20 % higher than that of pixel 25 (Fig. 4 (a)), and in fact we see a significantly improved separation of the first *p.e.* peak from the pedestal for that pixel . Furthermore, the gains extracted from the fits to the spectra of all 64 pixels of the CA4658 MAPMT are compared to those quoted by Hamamatsu in Fig. 5 (two channels are missing due to faulty electronic lines). In both cases, the values obtained from either the data or the Hamamatsu test sheet results have been calculated relative to the values for highest gain pixel determined by the Hamamatsu measurements. There is a very strong agreement between the two relative gain distributions for the pixels. For the top and bottom rows of the MAPMT (pixels 1 - 8 and 57 - 64 respectively), the curves match less closely with each other, however the agreement for these rows remains within ~20 %. The mismatch for these two rows may arise from an alignment issue, since the edge pixels have slightly larger dimensions, but only one step-size was used throughout the laser scans.

The results of the fitted parameters for all pixels of the MAPMT CA4658 are shown in Figs. 6 (a), (b), (c) and (d), where, from top left to bottom right, we can see:

- the normalisation constant A, which should correspond to the recorded events per pixel;
- the average number of detected *p.e.*, μ;
- the width of the Gaussian of the first *p.e.* peak, S_1, in QDC channels;
- the gain (in QDC channels) of the first *p.e.* peak, defined as the difference between the means of the first *p.e.* and the pedestal distributions.

For all pixels we found that, in general, the normalisation constant is equal to the total number of events (10^4) and that the average number of *p.e.* is roughly the same. These are both indications

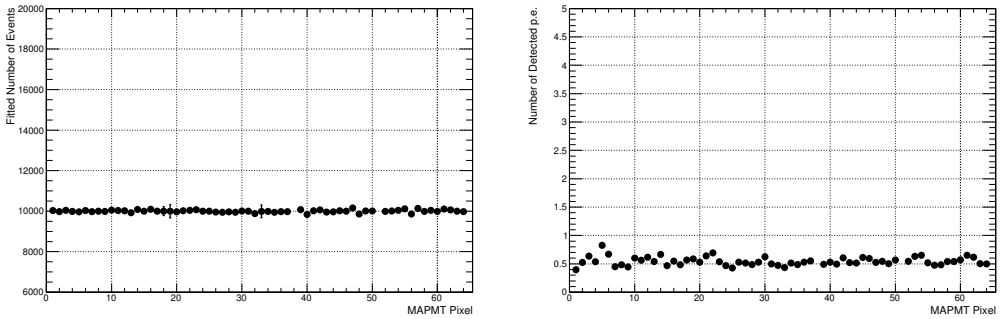

(a) Normalisation constant.

(b) Average number of detected p.e..

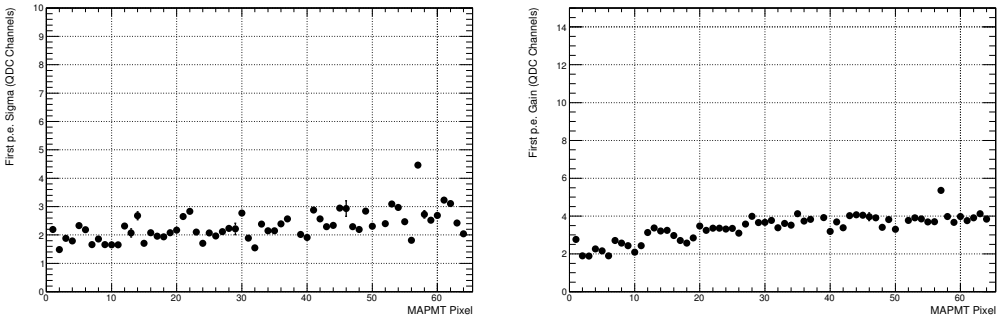

(c) Sigma width of the first p.e. peak.

(d) Gain of the first p.e. peak.

Figure 6: Pixel dependence of some of the fitted parameters for the CA4658 MAPMT spectra measured at HV=-1000 V.

of the reliability of the fitting procedure. There do exist a small subset of channels, corresponding to the pixels with smaller gains and thus with the first *p.e.* peak closer to the pedestal, for which the fit at 1000 V is not reliable, even if the the χ^2 of the fits is good (in most cases this was not exceeding 2). The slight increase of the measured gain as the pixel number increases is in agreement with the gain map provided by the Hamamatsu for this MAPMT (see Fig. 5).

To compare the uniformity of all 28 MAPMTs, the fitted gains extracted from each pixel of each MAPMT are shown in the distribution of Fig. 7 (electronic readout channels which were non-functional have been removed), where each pixel's gain has been calculated relative to the highest gain pixel of each MAPMT. The distribution is narrowly peaked, with an RMS of only ∼15 % extracted, which confirms an adequately small spread in the gains of the MAPMTs. If necessary such a gain dispersion may be easily compensated by standard front end electronics pre-amplifiers. The distribution of the fitted first p.e. peak widths ($S\,1$) is shown in Fig. 8 (a), where an RMS of ∼ 1 QDC unit is obtained, again indicating a consistent shape of the single p.e. peak. Fig. 8 (b) gives the ratio of first p.e. peak widths divided by their gains, which may give an indication of the spread in resolutions of the first p.e. peaks amongst the MAPMTs. The distribution is narrowly centred around 65 %.

To further summarise the results and compare the responses amongst different MAPMTs, we calculated the averages of the fitted parameters over the 64 pixels of each MAPMT at HV =

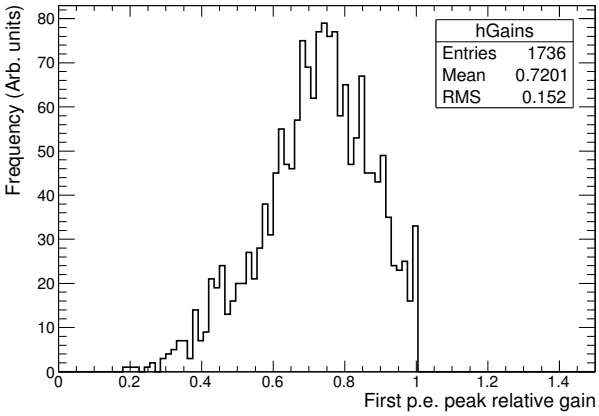

Figure 7: Fitted gain parameter extracted for each pixel of the 28 MAPMTs, normalised to the corresponding highest gain pixels.

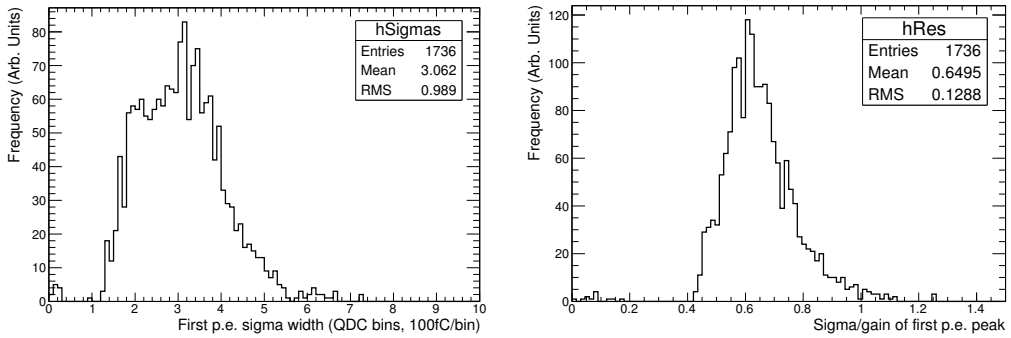

(a) First p.e. sigma width.

(b) First p.e. sigma width divided by gain.

Figure 8: First p.e. peak sigma width and sigma width to gain ratio values returned by the fitting function, for all pixels of the MAPMTs.

-1000 V. In Fig. 9 we show, for instance, the average absolute gains for the 28 MAPMTs under test (red circles for the 14 H8500C MAPMTs and blue squares for the 14 H8500C-03 MAPMTs), compared with the absolute gains obtained from the Hamamatsu test sheets. As seen, the agreement is very good.

5. Results at higher supply voltages

The measurements performed at the reference supply voltage of -1000 V have shown that the small separation between the pedestal and the first *p.e.* peak (typically a few QDC channels, see Fig. 6 (d)) makes the separation of the signal from the background difficult in some cases. Thus, we repeated all the measurements at different HV values: -1040 V and -1075 V, in order to study the behaviour of the MAPMT response as a function of the supply voltage.

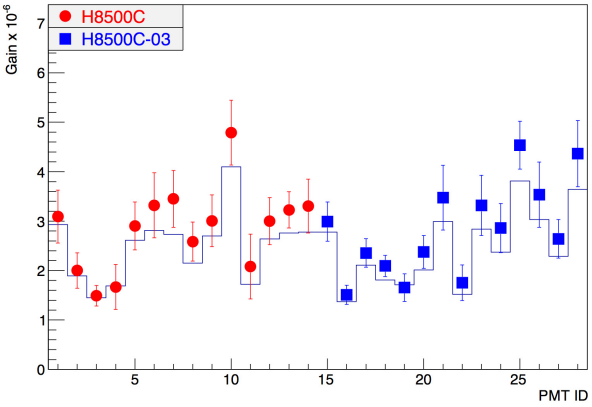

Figure 9: Average measured absolute gain at HV = -1000 V for the 14 H8500C MAPMTs (red circles) and the 14 H8500C -03 MAPMTs (blue squares) compared with the Hamamatsu test sheet values (histogram). The error bars represent the RMS values of the distributions of results for the 64 pixels of each MAPMT.

In Fig. 10, we compare the measured QDC distributions of pixel 36 (mapping to QDC channel 25) of the CA4658 MAPMT for the HV values of -1000, -1040 and -1075 V. The improvement in

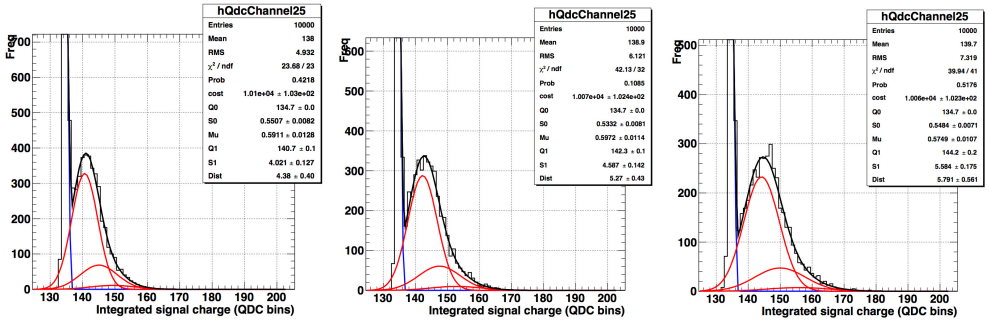

(a) 1000 V. (b) 1040 V (c) 1075 V

Figure 10: QDC spectra for pixel 36 (QDC channel 25) of the CA4655 MAPMT for HV=-1000, -1040 and -1075 V. The curves are the results of the fits, as in Fig. 4.

the separation of the signal from the pedestal as the gain increases is clear. The separation moves from 6 QDC channels at -1000 V to 9.5 QDC channels at -1075 V. As a further example, the relative increase in the gain at -1040 V and -1075 V with respect to the -1000 V measurements, for all the 64 pixels of the CA4658 MAPMT, is shown in Fig. 11. For the few results which are equal to or less than 1, this is due to a either faulty electronic channels or low gain pixels, where the fitting procedure was not as successful. On average, for all the 28 MAPMTs tested, the gain increase found at -1075 V was between 50% and 80% with respect to that at -1000 V.

The separation between the first *p.e.* signal from the pedestal is the crucial point for a single

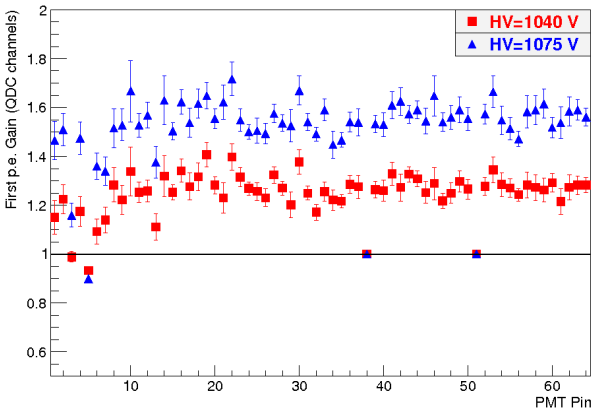

Figure 11: Relative gain for the 64 pixels of the MAPMT CA4655 at -1040 V (red squares) and -1075 V (blue circles) with respect to the measurements at -1000 V (horizontal line at value 1).

photon counting application such as the CLAS12 RICH detector. In fact, in the RICH detector, the occupancy will be no more than one photon per pixel, thus it is important that the fraction of the single *p.e.* spectrum below the pedestal peak is as small as possible. One can estimate this loss of events by integrating the gaussian fit of the one *p.e.* peak below a suitable cut selected to remove the QDC pedestal. Assuming a cut at $3\,\sigma$ above the pedestal peak, we obtained the results shown in Figs. 12 (a), (b) and (c), for the three supply voltages of -1000 V, -1040 V and -1075 V. We see that, at the highest voltage, except for one MAPMT, the average loss is below

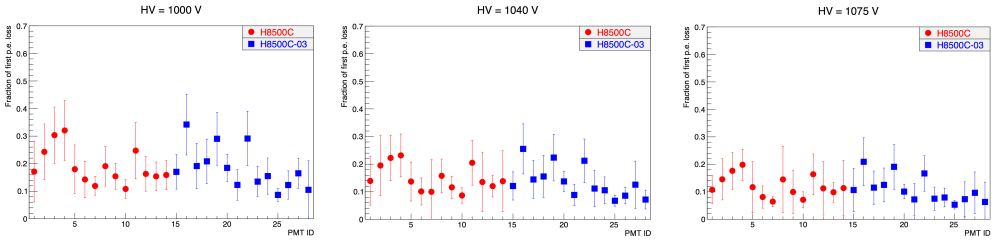

(a) 1000 V. (b) 1040 V (c) 1075 V

Figure 12: First *p.e.* peak fractional loss, estimated by integrating the gaussian fit of the first *p.e.* peak below a $3\,\sigma$ pedestal cut, at HV=-1000 V, -1040 V and -1075 V. Average values of all 64 pixels for each of the 14 H8500C MAPMTs (red circles) and the 14 H8500-C03 MAPMTs (blue squares) are given. The error bars represent the RMS of the distributions for the 64 pixels of each MAPMT.

20 % and that, within one RMS, almost all of the MAPMTs have a loss fraction below 30 %.

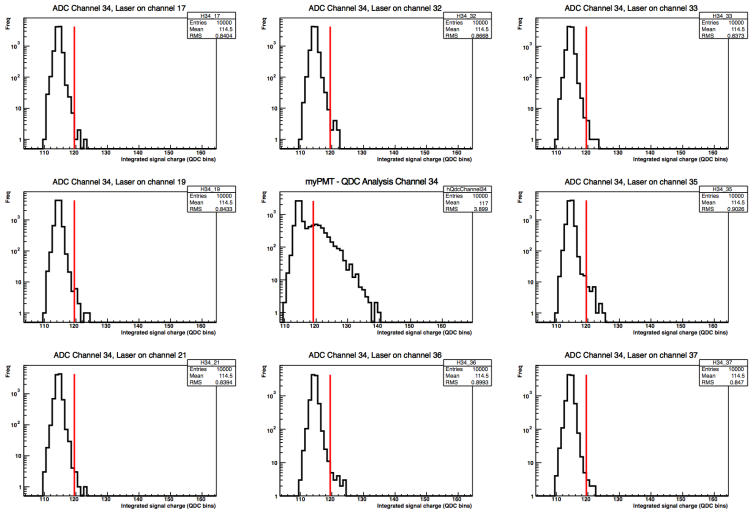

Figure 13: QDC distributions for one pixel of the CA4658 MAPMT when it is illuminated (central histogram) and when the laser strikes its eight neighbouring pixels, i.e. when it is not illuminated (surrounding histograms). The red vertical lines indicate the pedestal threshold cuts used.

6. Cross talk analysis

As previously described, in each measurement of a MAPMT and at a given supply voltage, only one pixel was illuminated by the laser at any time. The data from all 64 pixels, however, were simultaneously readout by the DAQ during each measurement, thus allowing an analysis of the cross talk between pixels to be made. The procedure is shown in Fig. 13. The cross talk levels shown here are higher than those intrinsic to the MAPMT since they likely include contributions from stray laser photons. Furthermore, we used the measurements taken at the HV setting of -1075 V to provide an upper limit for the measurements, since the cross talk magnitudes are expected to increase with HV.

We started by looking at the QDC spectrum of the illuminated pixel (central plot in Fig. 13) and we calculated the number of events above the pedestal threshold cut. Here, a pedestal threshold cut of $5\,\sigma$ was used to avoid including any possible fluctuations of the pedestal distributions. Then, we looked at the QDC spectrum of the same pixel when it was not illuminated, but when the laser struck one of its 8 adjacent pixels (4 side-sharing and 4 cornering neighbours), and again for each case we counted the number of events above the threshold cut in the spectra. As visible in Fig. 13, a small fraction of events above the threshold cuts may be recorded when the pixel is not illuminated, especially when the laser strikes the side-sharing neighbours. Such events are not due to electronic noise (compare with the pedestal shown in Fig. 3), but are caused by cross talk between adjacent pixels. Normalising the number of such events to the number of events above threshold when the pixel itself is illuminated, we calculated the cross talk probability for that given pixel from its adjacent ones. This is shown in Fig. 14 for the CA4658 MAPMT, where each one of the 64 pixels (except, of course, the ones on the geometrical edges of the MAPMT) can acquire cross talk hits from all 8 adjacent pixels. As seen, in average the cross

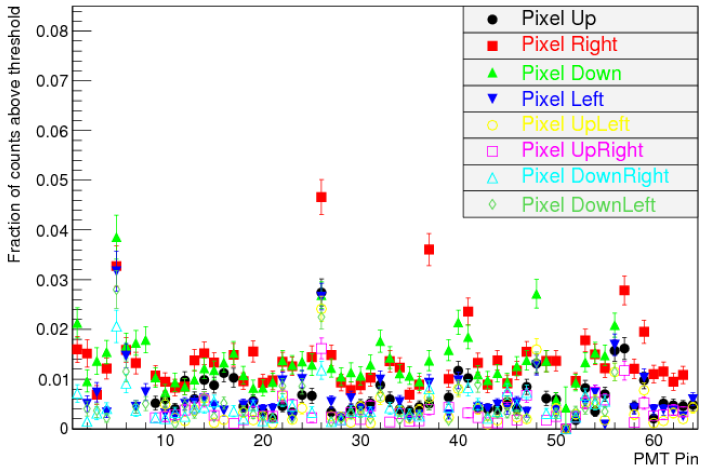

Figure 14: Fraction of cross talk hits for the 64 pixels of the CA4658 MAPMT when each of the eight adjacent pixels (up, down, left and right side-sharing neighbours and the 4 cornering neighbours) are illuminated.

talk values from each neighbour individually are less than 2% and the side-sharing neighbours typically contribute stronger cross talk than the cornering neighbours. This observation confirms the conclusion that the cross talk values observed are artificially increased due to stray light from the laser, since when illuminating the centre of a pixel without a mask, the side-sharing neighbours subtend a bigger solid angle than the cornering neighbours. From Fig. 14, no strong dependence upon cross talk direction within the side-sharing or cornering neighbours is observed.

Summing the cross talk contributions from the eight adjacent pixels, we obtain average cross talk levels of less than 8 % for all the tested MAPMTs. This is reported in Fig.15 (a), which shows the average values of the cross talk for all the MAPMTs tested, with the error bars again representing the RMS values amongst the 64 pixels of each MAPMT. In Fig. 15 (b), we show the average values of the cross talk as a function of the MAPMT dark current levels provided by the Hamamatsu test sheets (and as reported in Tab. 1). As seen, no dependence of the cross talk from the dark current appears to emerge, which again confirms that the dark currents of the H8500 MAPMTs are not a concern for their application to the RICH detector.

Again, the cross talk values obtained in this study represent an upper limit on the magnitudes, since the measurements were performed without use of a mask covering all MAPMT pixels, except from the illuminated one. Subsequent studies have shown that the incorporation of such a mask reduces the cross talk observed, due to the elimination of contributions from stray laser light. For example, Fig. 16 (a) shows the spectra of one pixel from the CA4686 MAPMT, again both when the pixel itself was illuminated and the cross talk spectra measured when the laser struck each of its eight neighbours. In Fig. 16 (b) we show the equivalent spectra obtained with the mask, where the number of counts above threshold when the laser strikes neighbouring pixels are visibly reduced. Summing the fraction of counts above threshold obtained when the pixel is not illuminated yields values of ≈ 4 % when no mask is used and ≈ 1 % when the mask is in place. It should be noted that this example represents one of the channels in which the effect was most visible. The cross talk probabilities for all pixels of the CA4686 MAPMT at 1075 V with

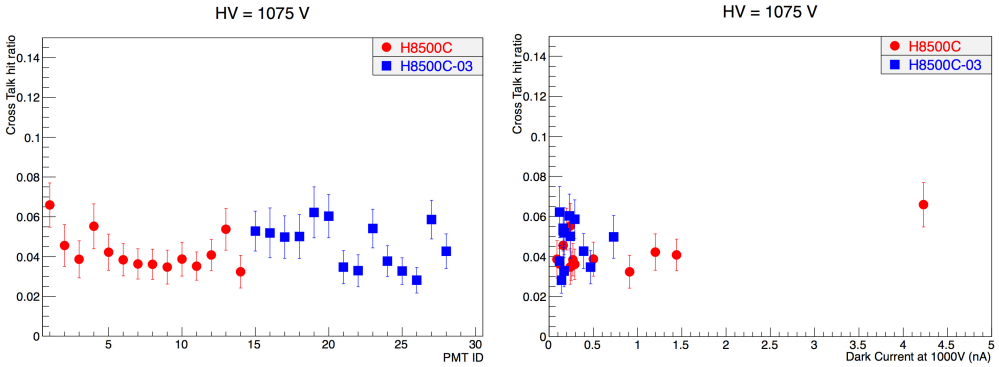

(a) (b)

Figure 15: (a) Average fraction of cross talk hits for the 14 H8500C MAPMTs (red circles) and the 14 H8500C-03 MAPMTs (blue squares, with the error bars representing the RMS values of the 64 pixels. (b) Average fraction of cross talk hits as a function of MAPMT dark current (from Tab. 1).

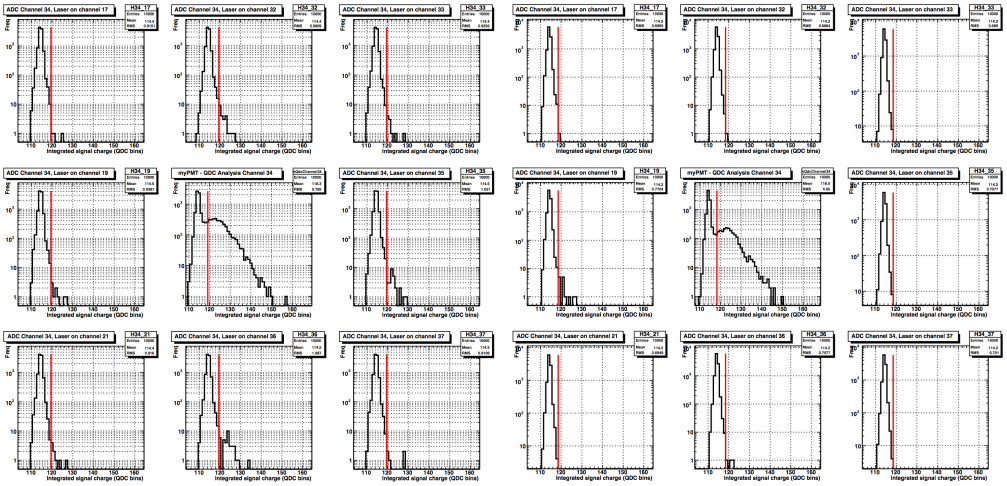

(a) (b)

Figure 16: QDC distributions for one pixel of the CA4658 MAPMT when it is illuminated (central histogram) and when the laser strikes its eight neighbouring pixels (surrounding histograms), (a) without and (b) with the use of a mask to eliminate stray laser photon contributions to the measured cross talk.

and without the mask in place are shown in Figs. 17 (a) and (b) respectively. As expected, the cross talk levels are mostly reduced when a mask is used, with the exception of some spurious points which likely arise due to a combination of the mask design and alignment issues.

It is concluded that, even based upon the slightly higher cross talk values measured without use of a mask, the MAPMTs are low cross talk devices and this noise source is not problematic

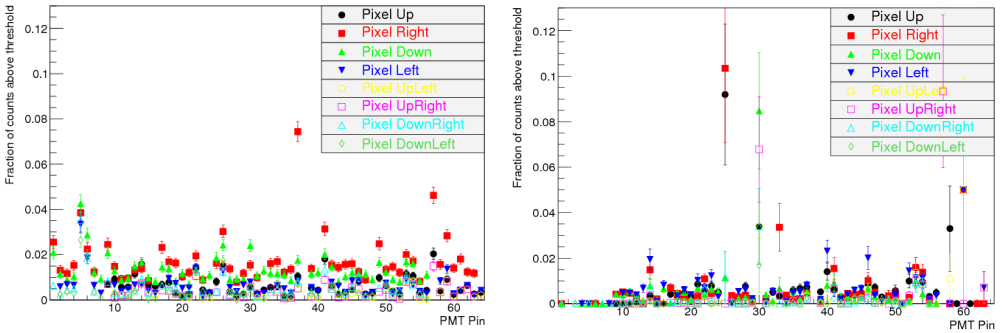

(a) (b)

Figure 17: Fraction of cross talk hits for the 64 pixels of the CA4686 MAPMT when each of the eight adjacent pixels (up, down, left and right side-sharing neighbours and the 4 cornering neighbours) are illuminated (a) without and (b) with the use of a mask.

for their use in the CLAS12 RICH detector.

7. Magnetic Field Studies

The positions of the RICH detector MAPMTs in the CLAS12 spectrometer are located within the fringe field of the torus magnet. Resultantly a very small field strength is anticipated, with a value of 3.5 Gauss expected from simulations in the worst possible case, for a only a few of the MAPMTs and in mainly the transverse direction. We studied the performance of an example H8500 MAPMT (CA4655) when placed within a magnetic field, ranging from strengths of 5 Gauss to 50 Gauss, to evaluate any degradation of its signal properties. At small field strengths, even which are larger than those expected in the CLAS12 RICH, no effect was observed in the MAPMT response within the sensitivity of the set-up, and only a negligible difference in the signals occurred at the largest value of 50 Gauss. Within an equivalent scope, the results are in agreement with previous studies of the H8500 behaviour in magnetic field environments [11].

The HV of the MAPMT was set to -1040 V for the duration of the tests, and laser scans were performed with and without the presence of the magnetic field. For this, the experimental set-up was modified to include a dipole magnet within the light-tight box. The arrangement and orientation of the dipole magnet used is shown in Fig. 18. The magnet was cylindrical in shape, with an outer diameter of $\sim$25.0 cm and an inner diameter of $\sim$8.5 cm, allowing the MAPMT to be fully inserted within the magnet. The magnetic field, which was roughly mapped before use using an external probe, was uniform in the vertical (Y) direction (transverse to the MAPMT axis) within 10 %, and negligible in the horizontal (X) and longitudinal (Z) directions. Within the 10 % uniformity, the field in the Y direction slightly increased towards the surfaces of the dipole coils. The upper limit for the field strength of the magnet was $B_Y = 50$ Gauss, where B_Y denotes the magnetic field strength in the vertical Y direction, and four field strengths in total were tested: 5, 10, 25 and 50 Gauss.

The standard fit function (Equation 1) was used to describe the spectra. Some examples of fitted spectra obtained from a typical inner pixel (pixel 28) at the different field strengths are shown in Figs. 19 (a), (b), (c), (d) and (e). As shown, the spectra were unaffected by the magnetic

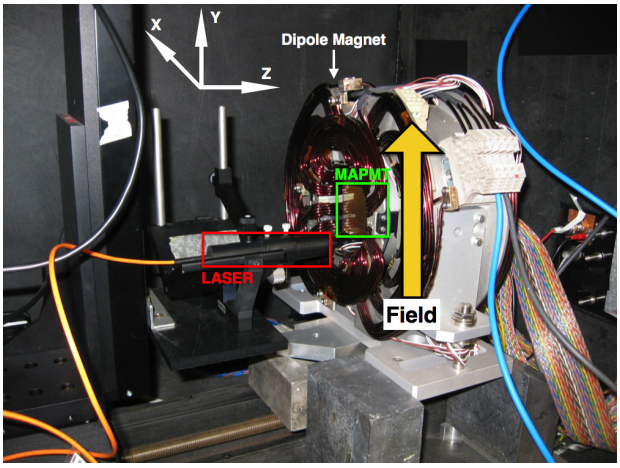

Figure 18: Set-up for the magnetic field tests. The MAPMT was placed completely inside a dipole magnet, with the orientation of the magnetic field transverse to the MAPMT axis.

field from 5 Gauss up to 25 Gauss and the pedestal and first p.e. peak fit parameter results were extremely stable. For the 50 Gauss setting a small increase in the number of events filling the valley region separating pedestal caused the fit to be marginally less successful in describing the amplitude of the first p.e. peak. This resulted in a reduction of the fitted gain which was on the order of only one QDC bin (100 fC), and was regarded as negligible. A similar behaviour was observed for the other inner pixels of the MAPMT and it was concluded that no major degradations in the signals were obtained. It was postulated that corner and edge channels of the MAPMT may be worse affected by the magnetic field. However, no strong deterioration was observed, as shown for a corner pixel of the MAPMT (pixel 64) in Figs. 20 (a), (b), (c), (d) and (e). Similar to the inner pixels' behaviour, the spectra obtained for the corner pixel at fields of 5, 10 and 25 Gauss were unaffected and only a negligible reduction in fitted gain parameter (here on the order of 2 QDC bins, or 200 fC) was obtained at the maximum field strength of 50 Gauss. A similar behaviour was observed in the remaining corner and edge pixels.

In Fig. 21 we show the gains extracted from fits to the spectra of all pixels of the MAPMT, at magnetic field settings of 5 and 50 Gauss and relative to the values obtained without magnetic field. The results for field strengths of 10 and 25 Gauss have been removed simply for clarity. There exist some points, in particular for edge channels where larger relative gains were extracted for cases with a magnetic field, however this is attributed to the success of the fit combined with the low-resolution spectra. For the majority of pixels the gain values were largely unaffected by the magnetic field of strength 5 Gauss, when fitting errors are considered, whereas reduced gains were observed for most of the pixels at 50 Gauss. This relative reduction was on average between $\sim 10\,\%$ and $\sim 20\,\%$, which corresponds to a difference on the order of 1 or 2 QDC bins. The results therefore do not indicate a significant problem for single photon counting with this MAPMT and field strengths ranging up to 50 Gauss. The fit results also do not show any strong distortion in the shapes of the spectra, as a function of magnetic field strength - Fig. 22 gives the sigma width of the first p.e. peak for all pixels, again at the field settings of 5 and 50 Gauss and relative to the values without field. Overall the shape of the signals were consistent, even up to a field strength of 50 Gauss. Where an effect is observed, in most cases these pixels are located

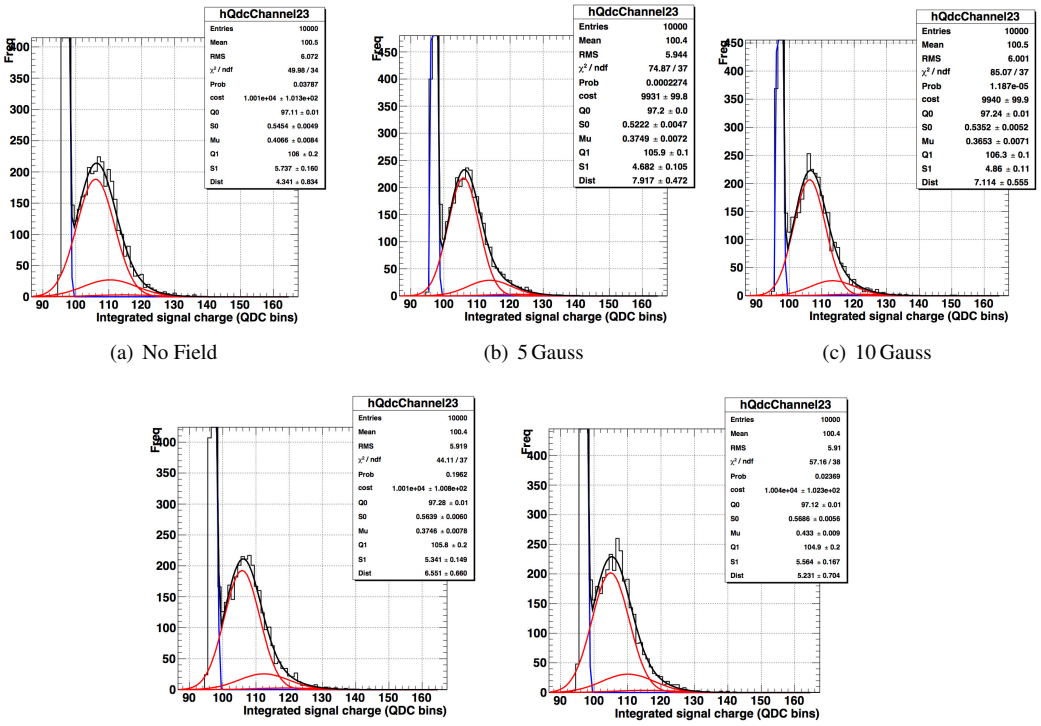

(a) No Field (b) 5 Gauss (c) 10 Gauss

(d) 25 Gauss (e) 50 Gauss

Figure 19: Fitted spectra obtained at the different magnetic field strengths for an example inner pixel of the CA4655 MAPMT (pixel 28, which mapped to QDC channel 23).

on the edge of the MAPMT (see Fig. 1) and the effect occurred at field strengths much larger than any expected in the CLAS12 RICH. Moreover, since the sigma widths of the first p.e. peaks were typically only a few QDC channels, even a relative fluctuation of 30 % corresponds to less than 1 QDC bin of difference and lies within the sensitivity of the fitting procedure.

The fit results averaged over all MAPMT pixels also demonstrated minimal dependence upon the tested magnetic field strengths. For instance, the averaged gain and sigma width parameters of the first p.e. peaks are shown in Figs. 23 (a) and (b), where the results have been separated into sub-sets depending upon the pixel locations on the MAPMT face. These averaged results illustrate more clearly a dependence upon pixel position, with edge and corner pixels being the most affected by the magnetic field. However, the deviation of the results for edge and corner pixels from those for the inner pixels lie within the 10 % uncertainty in the uniformity of the magnetic field, and therefore it is not possible to conclude whether this effect arises solely from the geometry of the pixels on the MAPMT face. The results averaged amongst all pixels simultaneously, independently from pixel position, are also given in the plots. Overall there is a reduction in the gains and shift in the widths of the first p.e. peak observed, the magnitudes of which are extremely small (on the order of 1 QDC bin) and therefore confirm that no significant deterioration in the single p.e. detection is observed even up to magnetic field strengths of 50 Gauss in the

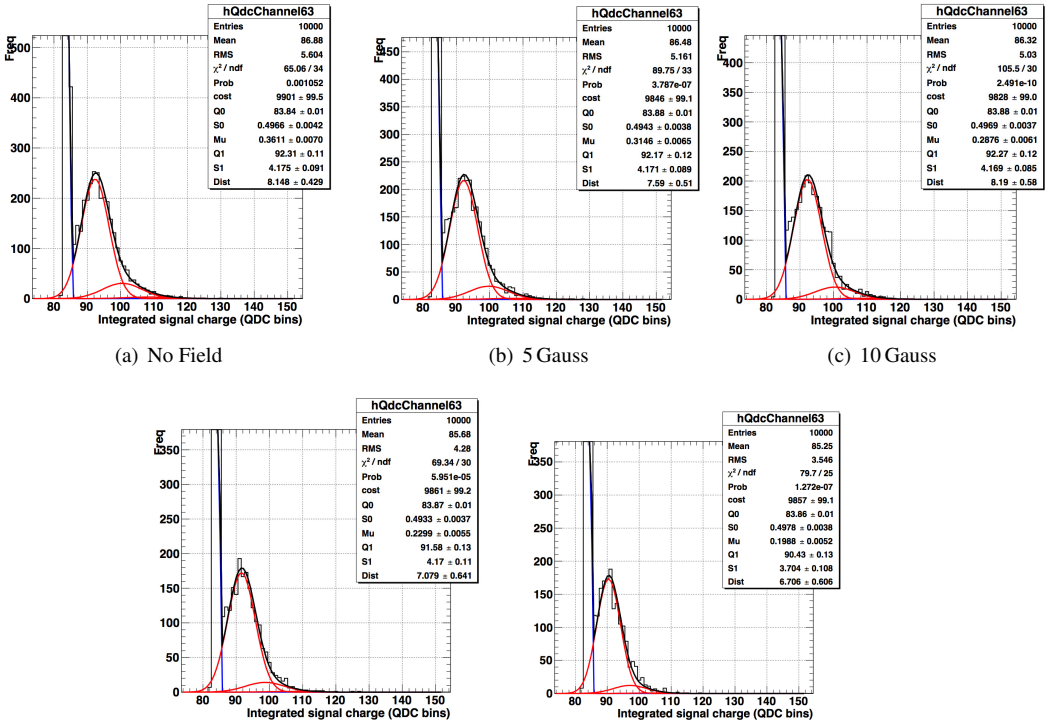

(a) No Field (b) 5 Gauss (c) 10 Gauss

(d) 25 Gauss (e) 50 Gauss

Figure 20: Fitted spectra obtained at different magnetic field strengths for an example corner pixel of the CA4655 MAPMT (pixel 64, which mapped to QDC channel 63).

direction transverse to the MAPMT axis.

It was also planned to study the effects of longitudinal magnetic fields, with respect to the direction of the MAPMT axis, since from previous studies of the H8500 MAPMT these fields are expected to have the strongest effect on its performance [11], however these studies were not possible with the set-up due to space restrictions. Moreover, the RICH MAPMTs will not be subjected to any longitudinal fields in CLAS12 and only small components in this direction are expected, which may arise from non-uniformities in the torus magnet and will not be large enough to affect the behaviour of the MAPMTs.

8. Conclusions

For the first time, a large statistics and significant sample of two different types of Hamamatsu H8500 MAPMTs (14 + 14) has been tested, pixel by pixel, using a dedicated laser beam, at different HV values and also within a (weak) magnetic field. The overall aim of these studies was to assess the performances of the H8500 MAPMTs as single photon detectors, in view of their use in a RICH detector. The results show that the Hamamatsu H8500 MAPMTs can be used successfully for such purposes, even if a voltage slighter higher than the recommended one

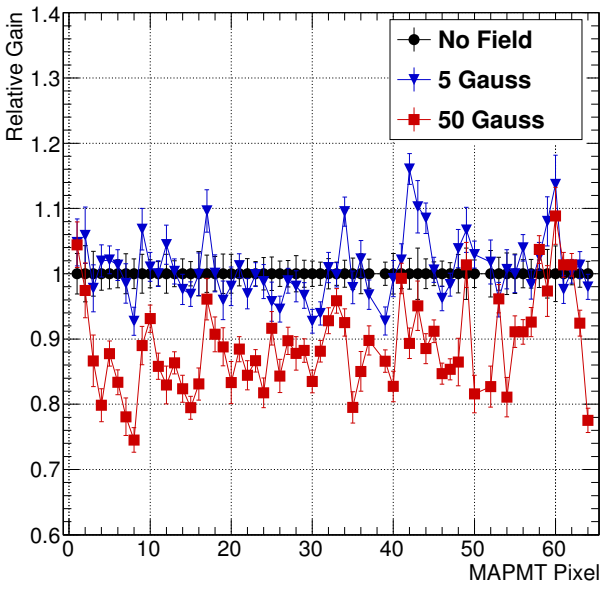

Figure 21: Gains of the CA4655 MAPMT pixels extracted from the fits to their spectra obtained at magnetic field strengths of 5 and 50 Gauss (blue triangles and red squares respectively), calculated relative to the values for no magnetic field (black circles).

(-1000 V) significantly improves their performances for single photon detection. Additionally, their performances are expected to be practically unaffected in the weak magnetic fringe field foreseen in the CLAS12 spectrometer.

These results, which agree with and expand upon what has similarly been reported for a smaller sample of the H8500 MAPMT [11], confirm their selection and suitability for use in a RICH detector for CLAS12.

References

[1] V.D. Burkert, *arXiv:1203.2373v1 [nucl-ex]*, 2012.

[2] B.A. Mecking *et al.*, Nucl. Ins. and Meth. in Phys. Research **A503** (2003) 513

[3] The CLAS Collaboration, CLAS12 technical design report, revised version, version 5.1, 2008. http://www.jlab.org/Hall-B/clas12_tdr.pdf [Last accessed 12/06/14].

[4] M. Contalbrigo *et al.*, Nucl. Ins. and Meth. in Phys. Research **A639** (2011) 502.

[5] Hamamatsu Photonics K.K., Flat Panel Type Multianode PMT Assembly, H8500 Series, Datasheet, www.hamamatsu.com [last accessed 12/06/14].

[6] Advanced Laser Diode Systems GmbH, The Picoseconds Laser Diode Systems, Datasheet, http://www.bbnint.co.uk/data_sheet.php?pdf=documents/pdfs/ALS/PiLas.pdf [last accessed 12/06/14]

[7] Thorlabs, Stepper motor controller and mototrised translation stages, Datasheets, http://www.thorlabs.de [last accessed 12/06/14].

[8] Edmund Optics, UV-VIS Neutral Density Filters, Datasheets, http://www.edmundoptics.com/optics/optical-filters/neutral-density-filters/uv-vis-neutral-density-nd-filters/2332 [last accessed 12/06/14].

[9] R.A. Montgomery *et al.*, Nucl. Ins. and Meth. in Phys. Research **A695** (2012) 326.

[10] E.H. Bellamy *et al.*, Nucl. Ins. and Meth. in Phys. Research **A339** (1994) 468.

[11] S.P. Malace *et al.*, 2013 JINST 8 P09004

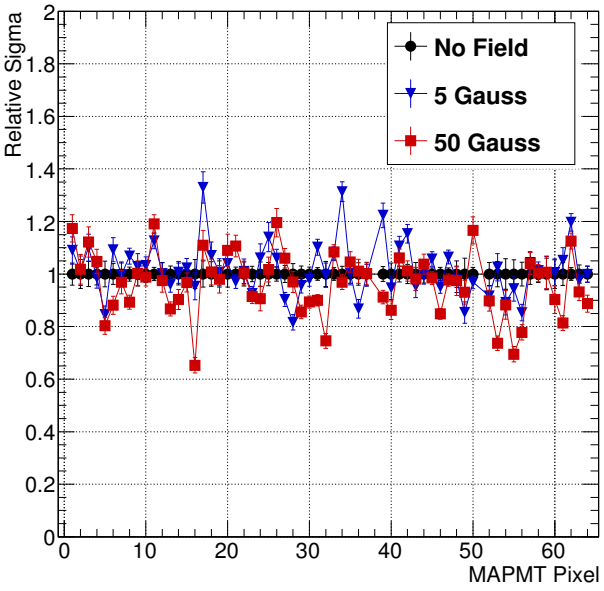

Figure 22: Sigma widths of the first p.e. peak of each pixels' spectrum at magnetic field strengths of 5 and 50 Gauss (blue triangles and red squares respectively), relative to the values for no magnetic field (black circles).

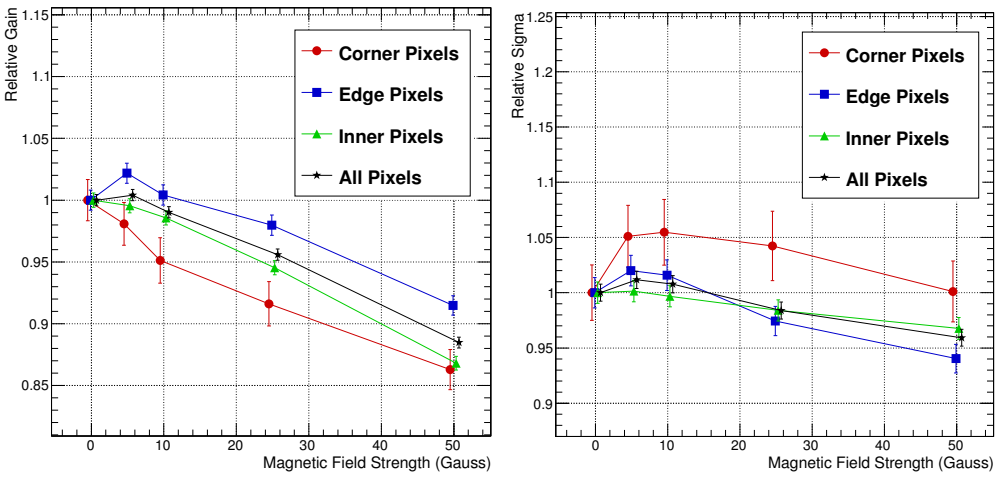

(a) First p.e. peak gain.

(b) First p.e. peak sigma width.

Figure 23: Average fitted first p.e. peak gain and sigma widths obtained at the tested magnetic field strengths. The results averaged amongst all pixels simultaneously are shown (black stars), in addition to sub-sets which have been averaged according to the geometrical positions of the pixels on the MAPMT face. The sub-sets are: 4 corner pixels (red circles); 24 edge pixels (blue squares) and 36 inner pixels (green triangles).